Photochemical & Photobiological Sciences
https://doi.org/10.1007/s43630-024-00558-x

ORIGINAL PAPERS

Characterization and evaluation of photolabile (μ-peroxo)(μ-hydroxo)bis[bis(bipyridyl)cobalt caged oxygen compounds to facilitate time-resolved crystallographic studies of cytochrome *c* oxidase

Emil Sandelin[1] · Jonatan Johannesson[1] · Ola Wendt[2] · Gisela Brändén[1] · Richard Neutze[1] · Carl-Johan Wallentin[1]

Received: 26 January 2024 / Accepted: 4 March 2024

Abstract

Photolabile (μ-peroxo)(μ-hydroxo)bis[bis(bipyridyl)-cobalt-based caged oxygen compounds have been synthesized and characterized by optical absorbance spectroscopy, X-ray crystallography. and the quantum yield and redox stability were investigated. Furthermore, conditions were established where redox incompatibilities encountered between caged oxygen compounds and oxygen-dependant cytochrome *c* oxidase (CcO) could be circumvented. Herein, we demonstrate that millimolar concentrations of molecular oxygen can be released from a caged oxygen compound with spatio-temporal control upon laser excitation, triggering enzymatic turnover in cytochrome *c* oxidase. Spectroscopic evidence confirms the attainment of a homogeneous reaction initiation at concentrations and conditions relevant for further crystallography studies. This was demonstrated by the oxidizing microcrystals of reduced CcO by liberation of millimolar concentrations of molecular oxygen from a caged oxygen compound. We believe this will expand the scope of available techniques for the detailed investigation of oxygen-dependant enzymes with its native substrate and facilitate further time-resolved X-ray based studies such as wide/small angle X-ray scattering and serial femtosecond crystallography.

Graphical abstract

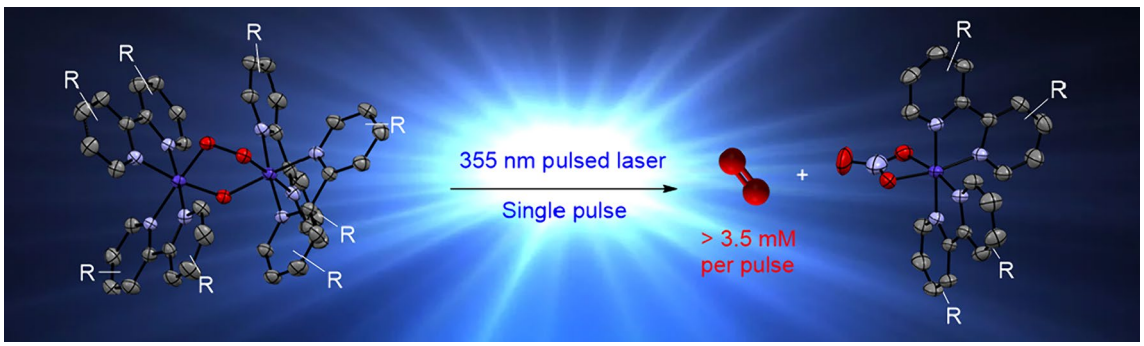

Keywords Caged oxygen · Cytochrome *c* oxidase · Time-resolved studies

✉ Carl-Johan Wallentin
carl.wallentin@chem.gu.se

[1] Department of Chemistry and Molecular Biology, The University of Gothenburg, Kemivägen 10, Gothenburg, Sweden

[2] Department of Chemistry, Centre for Analysis and Synthesis, Lund University, Lund, Sweden

1 Introduction

Oxygen is arguably one of life's most vital molecules, participating in a multitude of indispensable biological processes. In the realm of oxygen driven enzymatic reactions, those involving short-lived intermediates proceeding through an early oxo- or peroxo-intermediate, such as in cytochrome

Published online: 14 April 2024

P450 monooxygenase [1, 2], methane monooxygenase [3] and the heme-copper oxidase family [4, 5] have for long eluded detailed mechanistic study and structural elucidation. The fast time-scales at which these intermediates operate render traditional flow flash and mixing techniques inadequate for accurate detection [6–8]. Furthermore, traditional methods of studying such short-lived intermediates have relied upon methods for blocking the oxygen binding site with non-native ligands such as carbon monoxide. Applications of photolabile caged-oxygen carriers for time resolved studies of oxygen dependant enzymes have circumvented some conventional pitfalls associated with traditional flow flash techniques [6, 9]. Binuclear dioxygen bridged cobalt(III) complexes that have for long been known to release oxygen thermally, chemically and photochemically [10–13]. However, early bis(ethylenediamine)-based complexes were plagued by very poor photochemical quantum yields and exhibited low aqueous solubility, significantly hampering their utility in biochemical investigations [11]. More recently, a (μ-peroxo)(μ-hydroxo)bis[bis(bipyridyl) cobalt (HPBC) compound have been demonstrated to be a particularly versatile tool and have been successfully applied to time resolved spectroscopic studies of the quinol oxidase [14], bovine aa_3-type [6, 15] and the ba_3-type Cytochrome *c* oxidase [7, 15, 16]. The photoliberation reaction occurs at a rapid nanosecond time scale and produces molecular oxygen with high spatiotemporal control [17]. This type of controlled release addresses a significant challenge in studies which require a rapid reaction initiation prior to detection, such as pump-probe spectroscopic studies based on optical absorbance and similar experiments which use X-rays. The study of proteins and substrates in the field of structural biology has long sought out this possibility but a high degree of temporal control has been lacking for substrate dependent proteins and even innovative and sophisticated mixing approaches have struggled in achieving millisecond time resolution [18–21]. Photo-cages present a promising avenue for establishing temporal control in time resolved crystallographic experiments [22, 23]. Notably, three examples of X-ray crystallography-based studies involving a photolabile caged compound have been reported. These studies showcase the successful decaging of nitric oxide, ATP, and fluoroacetate in conjunction with their respective enzymes, leading to the acquisition of valuable structural information [23–26]. Here we set out to investigate if a caged oxygen compound could enable time resolved crystallographic studies of the ba_3-type CcO, a member of the heme-copper oxidase family. The structure of the oxidized state of ba_3-type CcO has been previously reported using serial femtosecond crystallography (SFX) [27, 28] and more recently, the time-resolved dissociation of carbon monoxide from the reduced carbon monoxide-bound state has been investigated [29]. However, to gain further structural insight, it is imperative to study the native substrate with the enzyme and current efforts are directed towards implementing a caged oxygen compound for time-resolved (TR) crystallographic studies of CcO. The success of this endeavour could provide a novel avenue for elucidating structural identity of the catalytic intermediates and could pave the way for similar studies of different oxygen-dependent systems. To enable a substrate-based TR-SFX study it is imperative that a sufficiently high concentration of the substrate is liberated on a shorter time scale than the reaction of interest, upon external stimuli such as by a single laser flash. This ensures that the reaction initiation is synchronous. In this work we provide appropriate and general conditions for the implementation of a photolabile caged oxygen carrier to trigger the native reaction cycle under conditions for crystallographic studies of cytochrome *c* oxidase, and with the required spatio-temporal control to facilitate further time resolved crystallographic studies.

2 Results and discussion

For a photocage to be suitable for biological applications, compatibility with the experimental conditions such as stability over time, temperature and other chemical components in the system is imperative. Currently, there are two well established methods for preparing the reduced state **R** of CcO: treatment with excess sodium dithionite (NaDt) [27] or a combination of sodium ascorbate and a mediator such as hexaammineruthenium(II) [6] or phenazine methosulfate (PMS) [30]. In contrast to prior studies [6] involving caged oxygen compound **1** (Fig. 1, b), where no significant degradation was observed, we observed a rapid degradation of compound **1** when exposed to both methods of reduction (Fig S4). Subsequent analysis determined that sodium dithionite and ascorbate lead to the degradation of **1** with an accelerated effect when a mediator was used in conjunction with the reductant. The rate of decomposition depends on the relative concentrations of compound **1** and the reductant, but nevertheless would restrict any experimental applications to a rapid mixing approach to avoid this detrimental side reaction. In pursuit of a mixing-free TR-SFX experiment, we initially embarked on an investigation to determine if compatibility with the reducing agent could be enhanced through structural modification of the caged oxygen compound.

2.1 Synthesis of substituted caged oxygen compounds

Compounds **1–7** were synthesized to investigate steric and electronic effects on the oxygen liberation, according to Fig. 1a. Ligands (2 equivalents.) were dissolved and added to a solution of a cobalt(II) salt, which was then oxygenated

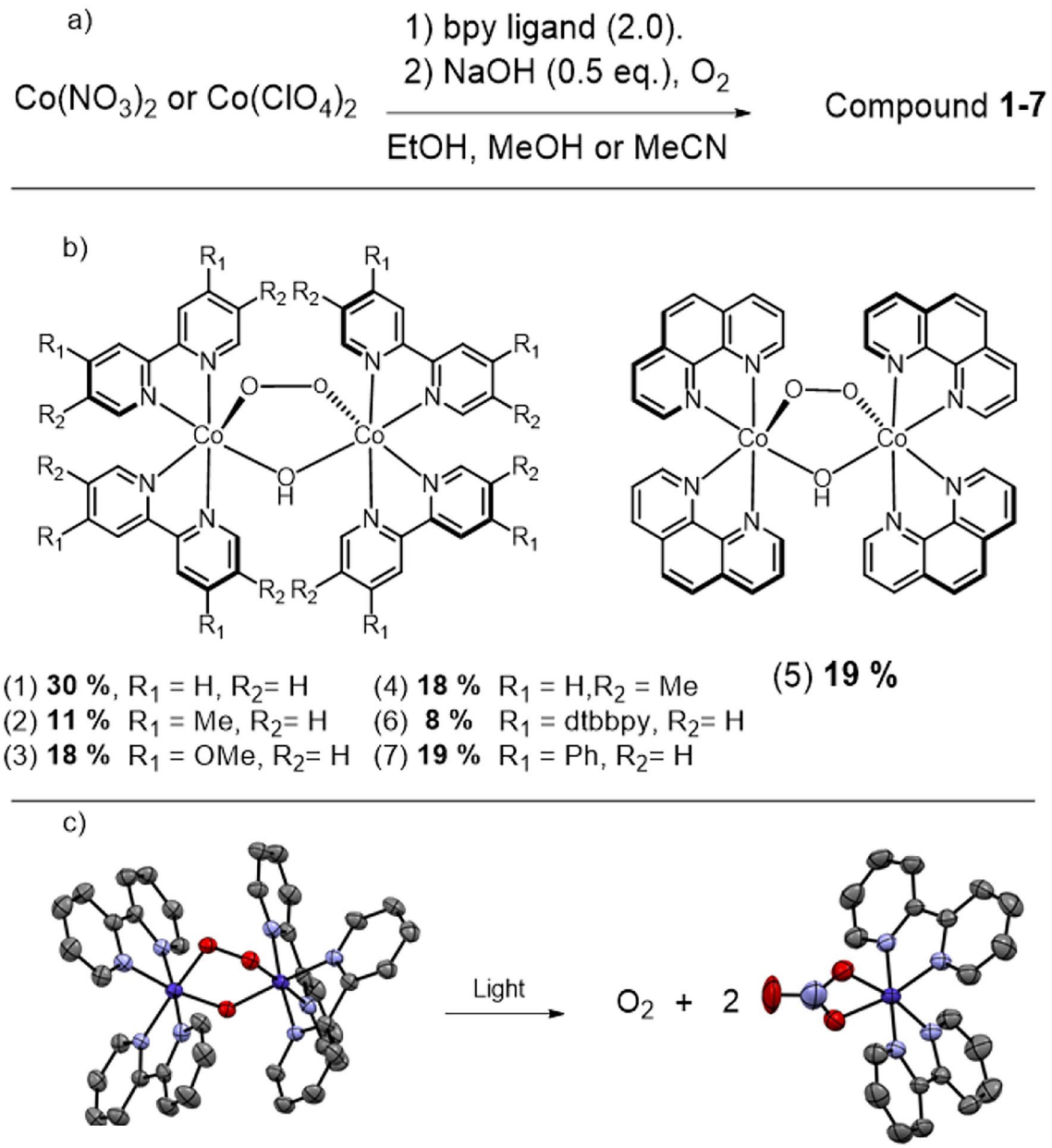

Fig. 1 **a** Overall reaction for the synthesis of compound **1**–**7**. **b** Structure and isolated yields of the produced HPBC complexes **1**–**7**. **c** The photoreaction of compound **1** illustrated with the ORTEP drawing of the crystal structures of compound **1** (left) and mononuclear cobalt(II) photoproduct (right). The nitrate counterions and hydrogens have been omitted for clarity. Compound **1**: triclinic, space group P-1. Photoproduct **1**: Monoclinic, space group C2/c. For CCDC depository numbers, see the Supporting Information.

with a slow addition of a hydroxide-base (0.5 equivalents.). The compounds were then isolated and purified by slow vapour diffusion. The previously described compound **1** was prepared with minor alterations to the original procedure [14] which in our hands generated a product with varying degrees of purity. Our adjusted protocol resulted in a lower yield but more consistently produced crystalline pure product.

Overall, the steric and electronic properties of the ligand were found to have a profound impact on both stability and the yield of isolation, which were generally low (Fig. 1b). Methylation at the para and meta-positions of the bipyridine ring (Fig. 1b, compound **2**, **4**) proved to be tolerated but not in the ortho-position (Fig S1, A). Sterically demanding ligands such as 1,1′-biisoquinoline (Fig S1, I) likely causes an unfavourable coordination angle to the metal in the final complex, while 2,2′-biquinoline (Fig S1, H) possibly suffers from unfavourable steric interactions due to substitution in the ortho-position. A para-methoxy substituted complex (Fig. 1b, compound **3**) is tolerated but the corresponding

hydroxyl-compound (Fig S1, O) was not, possibly due to increased solubility which likely prevents crystallization and isolation. Attempts to isolate by precipitating as either PF_6 or BF_4 salts were also unsuccessful. Phenyl and tert-butyl (Fig. 1b, compound **6**, **7**) substituents in the para-position are tolerated but this renders the complex insoluble in water, even as nitrate salts which typically have high aqueous solubility. The corresponding phenanthroline derivative could also be synthesized but suffers from poor aqueous stability and decomposes completely over several hours at room temperature (Fig. 1b, compound **5**). All attempts to synthesize and isolate electron deficient complexes were unsuccessful (Fig S1, B–F, J, L–N), possibly explained by the fact that the oxygenation reactions of μ-peroxo-μ-hydroxo cobalt(III) complexes are assisted by ligand to metal sigma donation that stabilizes the dioxygen adduct [31, 32]. An unexpected cubane-type side product was identified by X-ray crystallography, from the reaction with 4,4′-bis(trifluoromethyl)-2,2′-bipyridine (supplementary crystal structure 2). This indicated that electron deficient ligands might allow for non-productive alternative reaction pathways, in addition to a likely faster decomposition in solution. Compound **1** could reliably be prepared in higher yields as a tetra fluoroborate salt (47%) with slightly lower water solubility compared to the nitrate salt, or as the hexafluorophosphate salt (> 90%) which exhibits poor aqueous solubility. Similar attempts to precipitate substituted compounds **2**–**7** resulted in the formation of brown precipitates with low yields and varying degrees of purity. Prolonged storage of compounds **1**–**7** at room temperature in solution typically results in thermal degradation and release of oxygen and the formation of red crystals, identified as photoproduct mononuclear cobalt(II) specie (Fig. 1c) and precipitation of a yellow side products were identified to be the corresponding tris(bipyridine) cobalt(II) mononuclear complex (Fig. 2, f) which is a side product from the reaction.

2.2 Crystallography

Crystals, suitable for X-ray crystallography were obtained for the different compounds by slow vapour diffusion. Crystallization was carried out at temperatures between − 20 and − 20 °C in the dark to obtain crystals for the HPBC complexes and some crystallization was performed after exposure to light to also obtain the photoproducts, which are easily identified as red plates in contrast to the black crystals for the HPBC complexes when mixtures was obtained. All HPBC compounds exhibits the characteristic (μ-peroxo)-(μ-hydroxo)-bridge. Furthermore, we observe μ(O)-μ(O) bond distances consistent to other closely related μ-peroxo complexes [13, 33] and slightly shorter than the earlier ethylenediamine based complexes [34]. Relevant bond lengths and angles are summarized in supplementary Table 1. We were unable to produce crystals of sufficiently good quality for compounds **3** and **5**. However, the photoproduct for compound **3** was obtained (Fig. 2e).

2.3 Spectroscopic analysis

The optical absorbance spectrums for the water-soluble compounds **1**–**5** are shown in Fig. 3a and the non-water-soluble compound **6–7** in Fig. 3b. All compounds display a broad, moderately strong characteristic peak in the range of 390–450 nm arising from a $\pi^*(O_2^{-2}) \rightarrow d\sigma^*$ ligand to metal charge transfer (LMCT) band (Fig. 3a, b) [33]. This is consistent with similar μ-peroxo-μ-hydroxo-cobalt compounds previously described in the literature [35]. The infrared stretch frequencies around 830–850 cm^{-1} of the O–O bond also support the character of the O_2 as a peroxo-type ligand as opposed to the superoxide [36]. 5Me-substituted compound **4** exhibits a slight red shift of the 305 nm absorbance band compared to the unsubstituted compound **1**. Phenanthroline based compound **5** does not share the 300 nm absorbance band and instead shows a strong absorbance peak around 270 nm. The para-methoxy substituted compound **3** exhibits a minor blue shift of the 300 nm peak, accompanied by a slightly lower extinction coefficient in this region and a higher coefficient in the 400 nm region. All the HPBC based compounds produced in this work are photolabile and upon light irradiation will dissociate into the corresponding cobalt(II) mononuclear complex and release molecular oxygen, as illustrated in Fig. 1c. To verify the previously demonstrated correlation between the disappearance of the 400 nm charge transfer band in the absorbance spectrum and liberation of O_2, the water-soluble compounds **1**–**5** were illuminated with blue LED light (385 nm) and the oxygen concentration was measured over time. The dissolved oxygen concentration was measured using a fluorescence oxygen sensor (Ocean optics, NeoFox using the patch-based FOXY formulation) preparation of the sample. In Fig. 3c the absorbance spectrum for compound **4** is shown before (solid line) and after (dashed line) light illumination. The photolytic product for non-water-soluble compound **6** obtained by photolysis in MeCN was identified with X-ray crystallography to form the same type of mononuclear cobalt(II) complex as photolysis in water (see Supplementary crystal structure 1). This together with the similar absorbance spectrum changes (compare Fig. 3c, d) and visible bubble formation after exposure to light at higher concentrations shows that the same O_2 liberating reaction occurs in non-aqueous solvents.

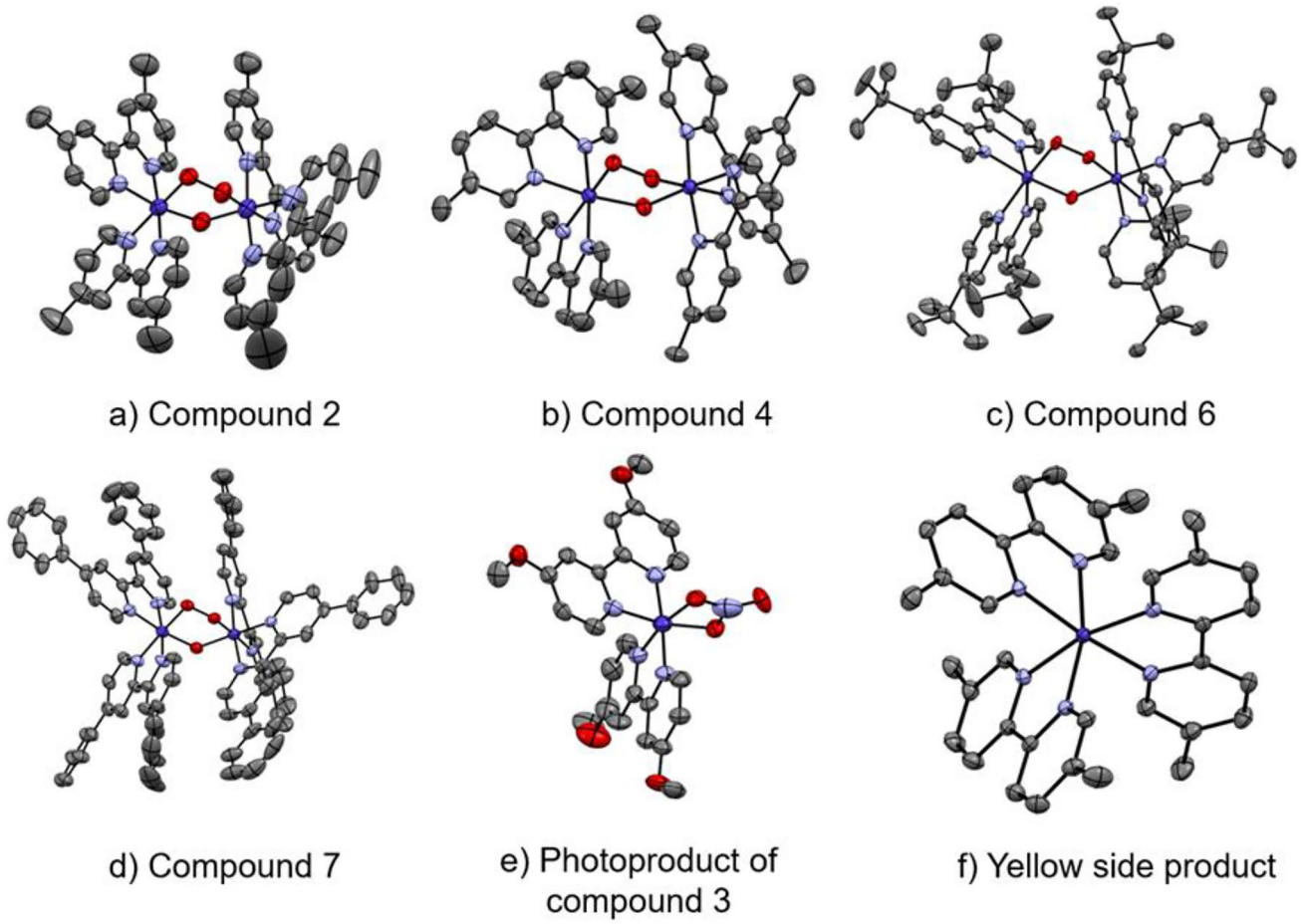

Fig. 2 ORTEP drawings of obtained crystal structures. Hydrogens, counterions and solvents have been omitted for clarity. For CCDC depository numbers, see the Supporting Information. **a** Compound **2**: monoclinic, space group $P2_1/c$. **b** Compound **4**: monoclinic, space group $P2_1/n$. **c** Compound **6**, triclinic, space group P-1. **d** Compound **7**, monoclinic, space group $P2_1/n$. **e** Photoproduct of compound **3** obtained by crystallization with NH_4BF_4 additive after exposure to light. Monoclinic, space group I2/a. **f** Yellow side product obtained during crystallization of compound **4**, triclinic, space group P-1

Table 1 Determined half-lives of compound 1–5 (5 mM) mixed with sodium ascorbate (5 mM) + PMS (1.5 µM) and sodium dithionite (5 mM)

Compound	$T_{1/2}$ (NaAsc + PMS)	$T_{1/2}$ (NaDT)	Peak anodic current (first reduction peak) (V)
(**1**) bpy	25 s	~0.8 s	− 0.23
(**2**) 4Me	19 min	20 s	− 0.34
(**3**) 4OMe	21 min	13 s	− 0.33
(**4**) 5Me	1 min	2 s	− 0.21
(**5**) Phen	7 s	~0.7 s	− 0.17
(**6**) 4dtbbpy	n.d.[a]	n.d.[a]	− 0.35
(**7**) 4Ph	n.d.[a]	n.d.[a]	− 0.27

The peak anodic current was measured for compound 1–7 (150 µM) with cyclic voltammetry in MeCN (NBu_4PF_6: 0.05 M) with a sweep rate of 100 mV/s. Values are reported vs Ag/AgCl reference electrode with a working electrode consisting of glassy carbon and a platinum counter electrode. The electrode was polished in between each run

[a]Not determined due to poor aqueous solubility

2.4 Reductant mixing and redox stability

Next, we probed the redox stability of the compounds **1–5** by exposing them to conditions typical for reduction of CcO. Employing a custom-built flow cell device [28] consisting of a 0.3 mm quartz capillary connected to a syringe pump, the time until 50% of the compound had degraded for compounds **1–5** was determined. Mixing was performed with 5 mM of compounds **1–5** and 5 mM of the reductant as this would be realistic reductant/oxygen cage concentrations for further studies. The stability of compound **1** could now be accurately determined and shows almost instantaneous decomposition when exposed to equimolar amounts NaDt (Table 1) and approximately 30 s half-life together with NaAsc + PMS. Although not completely detrimental for applications that can accommodate a very rapid mixing, this rapid degradation poses a significant challenge for the general use of caged oxygen compounds in crystallography-based studies. We rationalized that increasing the electron

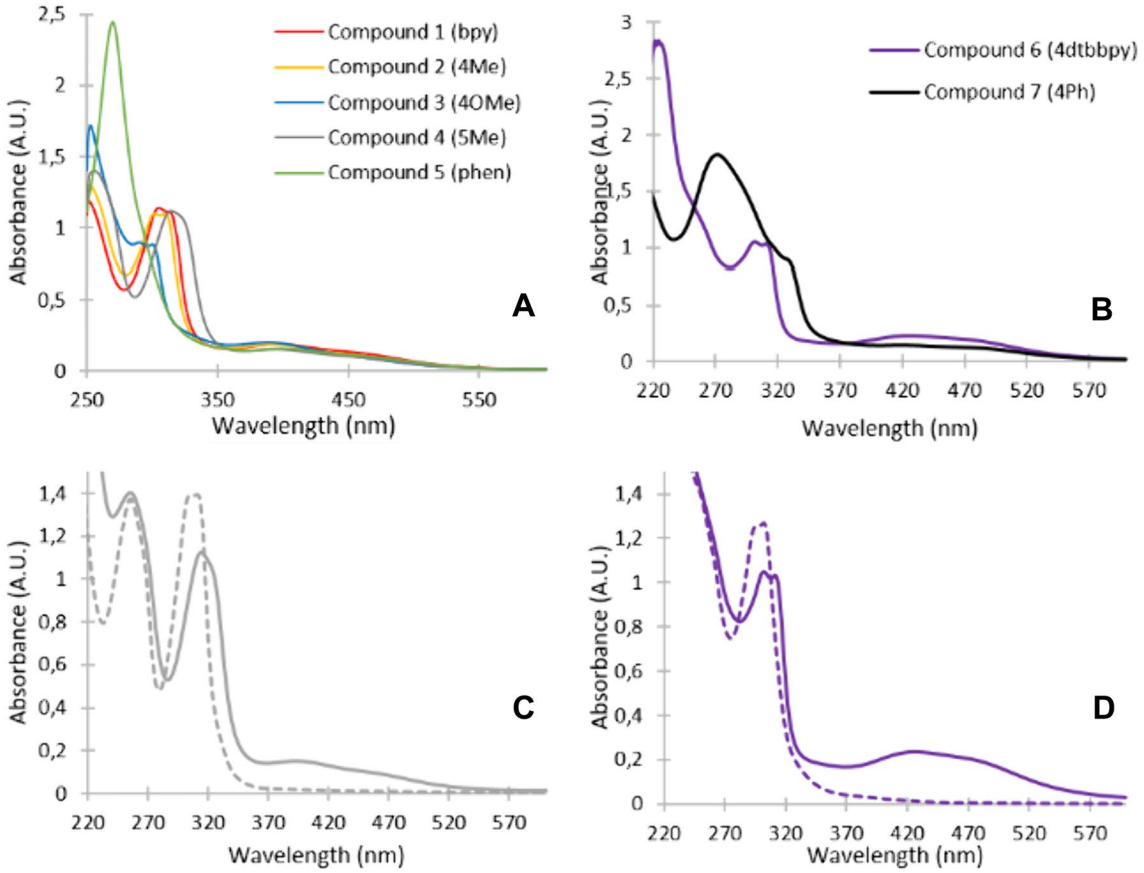

Fig. 3 **a** Absorbance spectrum of compound **1**–**5** (0.025 mM) in water. **b** Absorbance spectrum of compound **6** (0.025 mM) and **7** (0.0125 mM) in MeCN. **c** Absorbance spectrum of compound **4** before (whole line) and after (dashed line) photolysis in water. **d** Absorbance spectrum of compound **6** before (whole line) and after (dashed line) photolysis in MeCN

density of the cobalt centres by introducing an electron donating ligand would make the complex less susceptible to reduction and indeed compound **2**–**3** shows a significantly increased stability towards both reduction protocols, in addition to a significantly increased stability in solution at room temperature. Aqueous solutions of compounds **1,4** and **5** are not sufficiently stable at room temperature and will thermally degrade over several hours as opposed to compound **2** and **3**, which show only minor degradation over several hours. The peak anodic current was measured with cyclic voltammetry and the voltammograms for compound **1**–**7** were obtained in MeCN. The obtained voltammograms are complex with multiple irreversible processes contingent on the scan range and direction but we found that the first reduction peak, which disappeared upon subsequent cycles, correlated well with our stability study, and was observed for compound **1**–**7**.

The potential was also within a reasonable range (− 0.4 to − 0.2 V) compared to the reduction potential of relevant reducing agents. The peak anodic current was determined and a lower negative peak anodic current for the first reduction peak in the voltagram was found to be consistent with a compound more resilient towards chemical reduction (Table 1).Compound **5** shows an increased susceptibility towards chemical reduction which can be attributed to electronic factors, given that phenanthroline is a worse electron donor than bipyridine [37]. Compound **4** also falls under this category as a worse electron donor than compound **3** and **4** but is expected to be a slightly better donor than compound **1** which correlates well with the observed stability profile. Intrigued by the possibility of investigating further electron rich ligands, we first decided to evaluate the correlation between ligand electronics and the photolytic properties prior to such a commitment into further synthetic efforts as we suspected that the electronics would also influence the photo physical properties.

2.5 Photophysical properties and quantum yield

Preliminary photolysis experiments with the nitrate and the perchlorate salt of compound **1** raised concerns about the accuracy of some reported quantum yields. A prior study

claimed a wavelength-dependent quantum yield, correlating to the extinction coefficient, with reported quantum yields ranging between 0.2 and 0.5 for wavelength between 300 and 320 nm, and a significantly higher overall quantum yield than our findings [14]. This is in contrast to the previously determined quantum yield of 0.04 at 355 nm for the perchlorate salt [6, 17]. Upon re-evaluation of the quantum yield for compound **1**, it was discovered that the nitrate, perchlorate and tetrafluoroborate salts exhibited identical photolytic properties when illuminated across various wavelengths. The photon flux for several wavelength were determined by chemical actinometry using the well-established protocol for potassium ferrioxalate [38]. Our results align with first published quantum yield for the perchlorate salt [17] with quantum yields ranging 0.03–0.06 depending upon excitation wavelength (Table 2).

Surprisingly, we observed a decrease in quantum yield for compounds **2**–**7** compared to unsubstituted **1** across all investigated wavelengths. All compounds exhibit a higher quantum yield in MeCN compared to water, however, the stability of compounds **1** and **5** were significantly compromised in MeCN. These findings suggested to us that the relatively poor quantum efficiency of the photo-liberation reaction is an inherent property of HPBC based compounds

Table 2 Quantum yield of compound **1**–**7** in water and MeCN

Compound	Selected absorption[a] [nm and (ε)]	Quantum yield (φ) in water	Quantum yield (φ) in MeCN
(1) bpy	396 (7700)	0.04[b]	0.07[b]
	313 (44,500)	0.06[c]	0.19[c]
	305 nm (45,600 M^{-1} cm^{-1})	0.04[d]	0.19[d]
		0.03[e]	0.13[e]
(2) 4Me	392 (7600)	0.02[b]	0.05[b]
	310 (44,000)	0.02[c]	0.08[c]
	302 (44,000 M^{-1} cm^{-1})	0.02[d]	0.08[e]
	253 nm	> 0.01[e]	
(3) 4OMe	389 (8000)	0.02[b]	0.06[b]
	300 (35,000)	0.02[c]	0.10[c]
	291 (36,000 M^{-1} cm^{-1})	0.02[d]	0.08[e]
	253 nm	> 0.01[e]	
(4) 5Me	394 (6100)	0.02[b]	0.07[b]
	324 (42,300)	0.02[c]	0.08[c]
	315 (44,700 M^{-1} cm^{-1})	0.03[d]	0.12[e]
	256 nm	0.01[e]	
(5) phen	398 (6100 $M^{-1}cm^{-1}$)	n.d[f]	n.d[f]
	270 nm		
(6) 4dtbbpy	427 (9400)		0.02[b]
	311 (41,200)	n.d[g]	0.04[c]
	302 (42,000 M^{-1} cm^{-1})		0.04[e]
	225 nm[h]		
(7) 4Ph	420 (11,400)		0.03[b]
	328 (71,300)	n.d[g]	0.03[c]
	272 (145,000 M^{-1} cm^{-1})		0.03[e]
	215 nm[h]		

[a]At local absorption maximum

[b]Using 302 nm monochromatic light

[c]Using 334 nm monochromatic light

[d]Using 355 nm monochromatic light

[e]Using 392 nm monochromatic light

[f]Observed significant decomposition in solution at room temperature

[g]Not soluble

[h]Measured in MeCN

and further structural modification is unlikely to improve the quantum yield significantly. We therefore turned to a different approach to find compatible conditions by identifying an alternative method of producing the reduced state for cytochrome *c* oxidase. By identifying less reductive conditions we reasoned that the slightly more redox resilient compounds **3** and **5** could overcome the previous chemical incompatibilities or simply the generic use of any HPBC based compound.

2.6 Photoliberation of oxygen

After an exhaustive search for less reducing conditions, we identified that a substantial excess of dithiothreitol (DTT) could produce CcO in the fully reduced state **R**. However, this process exhibited a significantly slower reduction kinetic compared to traditional methods, taking several minutes rather than sub-second duration that is typically observed. Notably, the addition of a fourfold molar excess of DTT to compound **1** did not lead to any discernible acceleration of decomposition, which was confirmed by NMR (Fig S5) and optical absorbance spectroscopy (Fig S6). Encouraged by the discovery of less reducing conditions for preparing the active state of the enzyme, we could turn our attention to establishing a protocol that would enable time resolved crystallographic study of CcO. In previous time resolved spectroscopic studies where molecular oxygen or caged oxygen has been utilized, a 30–45 fold excess of released oxygen was employed [7, 15]. In crystallographic studies, the concentration of protein prior to crystallization is typically in the domain of 50–80 µM. For example, once crystals of CcO form [27], the concentration of protein within microcrystals is 2.3 mM. The inhomogeneous distribution of protein within the total sample means that to achieve a homogenous reaction initiation, two primary criteria must be satisfied; (1) 2–3 mM photoproduced oxygen should be liberated upon a single laser excitation and, (2) the validation of retention of time resolution at these concentrations, meaning that one can distinguish between the different reaction intermediates during oxygen-initiated turnover of the enzyme. Efficient oxygen liberation is crucial. To assess whether a HPBC compound could deliver this high concentration upon a single laser pulse, different concentrations of compound **1**, ranging from 1 to 30 mM, underwent exposure to a single 355 nm laser pulse (5 ns, approx. 2 mJ/pulse). The concentration of liberated oxygen was determined by the loss of absorbance at 400 nm, promptly recorded after each pulse. The experimental setup was designed to closely resemble the sample delivery and reaction initiation setup during a realistic X-ray based experiment (see SI) [28]. A thin quartz capillary (0.3 mm) connected to a syringe pump was used and we investigated if the required > 3 mM oxygen could be generated upon a single 355 nm laser flash. The selection of wavelength is motivated by general availability and that we envisioned that light penetration into the sample would be suitable at this wavelength. The importance of light penetration for homogeneous reaction initiation has been emphasized in previous studies [23, 39]. Our experiment shows that oxygen concentrations exceeding 3 mM could be achieved upon a single 355 nm laser pulse (Fig. 4). This corresponds to a concentration of O_2 13 times higher than the normal air saturated water and 3 times higher than pure O_2 saturated aqueous solution [40]. Concentrations above this level are considered to be supersaturated and will eventually lead to formation of bubbles. Supersaturation is reached because the diffusional escape of gas is slower than the timescale of photoliberation of O_2 [17, 41]. While bubble formation was occasionally observed, it did not negatively impact the measurements by upstream O_2 contamination or discontinuous flow. We, therefore, reason that oxygen concentrations locally will exceed the required 3 mM minimum during the timescale of the experiment since laser initiation would be followed quickly after by an X-ray pulse. While one might expect that a higher concentration of the compound would correlate with a greater oxygen release, our results revealed an optimal concentration threshold. Specifically, we observed an inner filter effect, characterized by a high optical density, at concentrations exceeding 7 mM, beyond which the photolytic oxygen yields plateaued and ceased to increase with higher concentrations of compound **1**. Conversely, at concentrations below 3 mM, the compound achieved full photolytic yield, indicating that even higher yields might be possible with a thinner capillary or by optimizing the laser illumination to encompass multiple angles.

Moreover, the use of thin jets, with diameters less than 100 µm, a common practice in viscous jet-based SFX

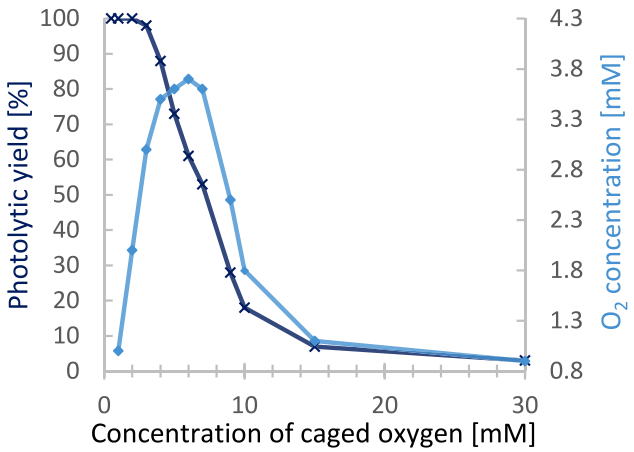

Fig. 4 Photoreleased O_2 upon a single 355 nm laser pulse (~ 1 J/cm^2, 5 ns pulse) showing the percentage yield (dark blue) and the molar yield (blue) of released oxygen. Collected inside a 0.3 mm quartz capillary with approximately 0.01 mm thick walls

experiments, could potentially enhance the oxygen concentration further when combined with multi-angle laser exposure. Encouraged by these results we moved on to simulate the conditions that would be realistic for a crystallography-based experiments.

2.7 Time-resolved spectroscopy

Typically, proteins can also absorb light in the 355 nm region and it is anticipated that this absorbance will decrease the photolytic yield of O_2 due to competing absorption of the light. We, therefore, reasoned that there is a high probability that the liberated oxygen to protein ratio during crystallographic conditions will be lower than previous spectroscopic studies. A caged oxygen/protein ratio of 20 was selected as we reasoned that this would be realistically achievable and would showcase a worst-case scenario when the O_2 could be a limiting factor. Time resolved optical difference spectra were recorded after a mixture of DTT reduced CcO and compound **1** in solution was exposed to a laser flash and the optical absorbance difference spectrum was recorded 2–2000 µs after the laser pulse (Fig. 5). Occasionally during the preparation of the sample, protein oxidation occurred prematurely. This was attributed to the slow thermal degradation of caged oxygen compound **1** when the sample was left for a prolonged time.

At higher concentrations this would outcompete the DTT mediated reduction, which is slow at lower pH. This occurs because DTT will be protonated to a higher extent, limiting its reducing capability, and effectively lowering the concentration of active reductant in the system. To mitigate this, a catalytic oxygen scavenger system [42] consisting of glucose oxidase, catalase and glucose was introduced to counteract the slow oxygen leakage. This prevented premature oxidation of the protein whilst not interfering with the kinetic binding of oxygen significantly. We obtained difference signals after laser excitation, consistent with the reaction of the reduced enzyme and molecular oxygen, which was achieved with a sufficient population to distinguish between various reaction intermediates (which is shown in Fig. 5) [16]. Notably, the first intermediate in the cycle, intermediate **A**, which occurs 5–10 µs after O_2 binding [7, 9] remains unresolved in our experiment, possibly due to limitations in time resolution. The integration time of the spectrophotometer (30 µs) together with a pulse tail from the light source (≈ 10 µs) leads to less resolved populations for short lived intermediates. Following oxygen ligation, the O–O bond is broken and this results in oxidation of heme a_3, which leads to a decrease in the difference spectrum at 445 nm and increase at 410 nm [9]. This is seen together with the oxidation of heme *b*, a decrease at 560 nm and increase at 610 nm, suggesting that a mixture of the intermediate **A** and the initial formation of $\mathbf{P_R}$ can be seen during the 2–10 µs time interval (Fig. 5A, B). The subsequent 50 µs time point exhibits well resolved characteristic spectral features for the formation of ferryl intermediate seen as $\mathbf{P_R}$ [15]. The highest population of $\mathbf{P_R}$ is detected at this time point (Fig. 5A, B). Following the formation of $\mathbf{P_R}$, is the re-reduction of heme *b* by Cu_A forming the **F**-intermediate, whilst also protonating the binuclear centre [9]. This should result in complete reduction of heme *b* and the disappearance of the negative peak at 560 nm [9]. However, rapid reduction of the formed **F**-intermediate likely results in mixed populations of **F** and the oxidized state of the enzyme during our measurements. The 100 µs time point shows re-reduction of heme *b*, determined from the 560 nm peak that is re-oxidized upon the 200 µs time point (Fig. 5D). The following time points between 500 µs and 2 ms shows the final transition from the mixed **F** state to the oxidized state shown by complete disappearance of the transient 610 nm positive peak. (Fig. 5E, F). We estimate that the reaction is initiated in approximately 40–45% of the total protein content by the laser pulse, leading to a reaction initiation homogeneous enough to clearly distinguish the $\mathbf{P_R}$ reaction intermediate. Increasing the concentration of caged oxygen and performing the laser illumination from more than one angle will likely lead to an even higher protein turnover yield/pulse.

Our protocol can successfully turn around the enzyme upon a single laser pulse, but the question remained if this would be possible to apply to a crystalline sample. With the added complication of a non-aqueous medium as the crystals are based on a liquid cubic phase (LCP) medium [43]. A LCP type phase is also commonly what is used for viscous sample injection during based SFX experiments [44]. We found that exposing an LCP sample containing DTT (15 mM) CcO microcrystals (3–6 µm, 50–60 µM) treated with the oxygen scrub protocol, and compound **1** (2.5 mM) to a single 355 nm pulsed laser produced a spectrum consistent with the transition from reduced state to oxidized CcO (Fig. 6). This was performed with our in-house flow cell using a 0.3 mm quartz capillary. Although a clean spectrum was not obtainable due to issues with light penetration, sample homogeneity and turbidity of the LCP phase, a difference signal consistent with oxidation could be obtained which consistently showed after multiple alternating dark/light cycles under flow conditions. A shift in the soret peak maximum from 425 nm towards 412 nm, consistent with oxidation was observed after 1 ms. A high flowrate was used, and no further significant change associated with protein oxidation was observed even after multiple laser pulses with a stationary sample was illuminated with multiple pulses.

A separate experiment was performed to investigate the ferryl-intermediate $\mathbf{P_M}$ in more detail, which as opposed to the $\mathbf{P_M}$ intermediate in other type oxidases [45], cannot be artificially isolated in a stable form by chemical means in the ba_3-type oxidase. This was performed by first producing the

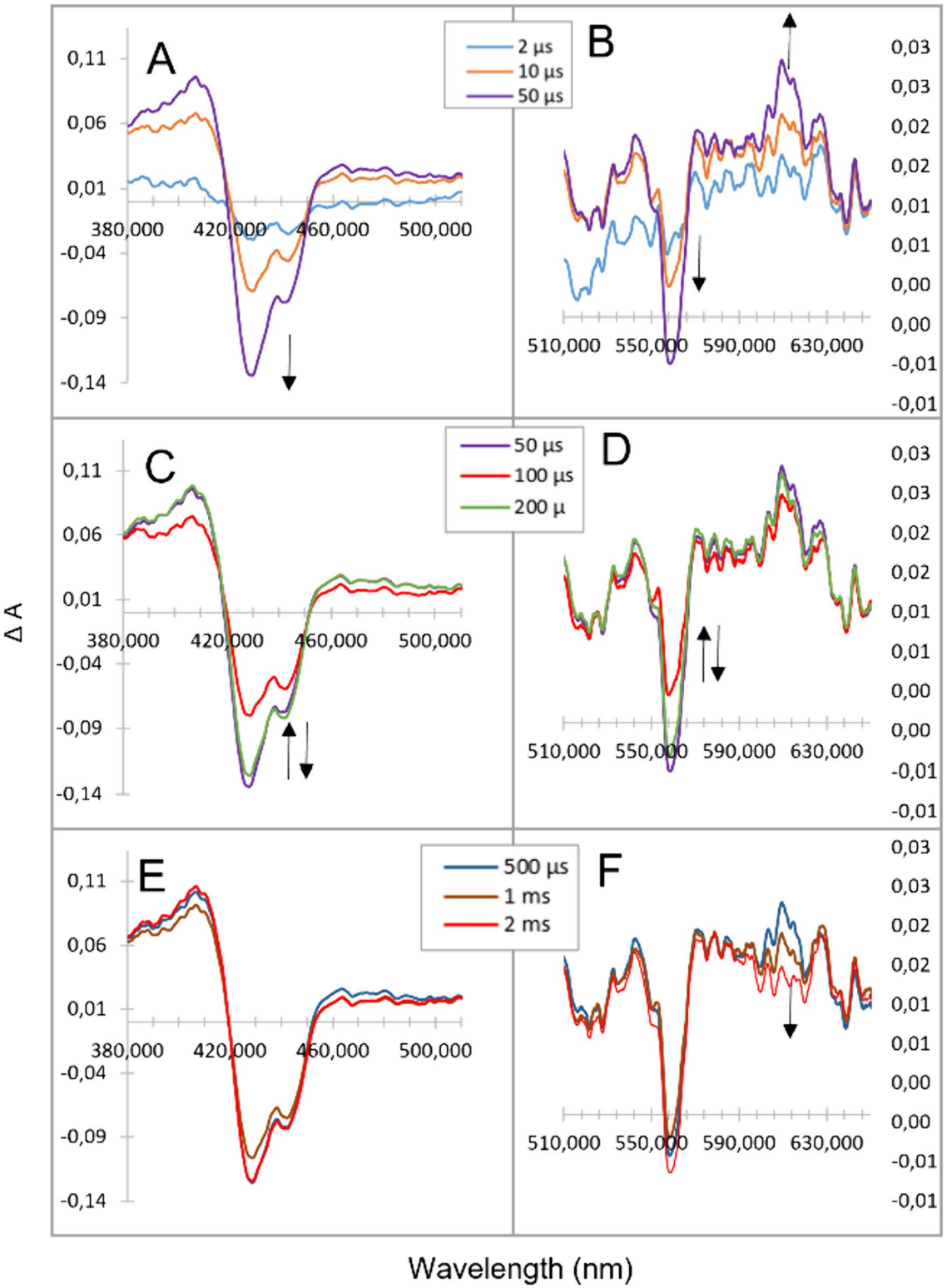

Fig. 5 Time resolved optical absorbance difference spectrums of DTT reduced CcO (120 µM) and compound 1 (2.5 mM) 2, 10, 50, 100, 200, 500 µs, 1 and 2 ms after a 355 nm laser pulse. The spectral contribution of compound 1 has been removed and the reduced protein + compound 1 was used as the blank

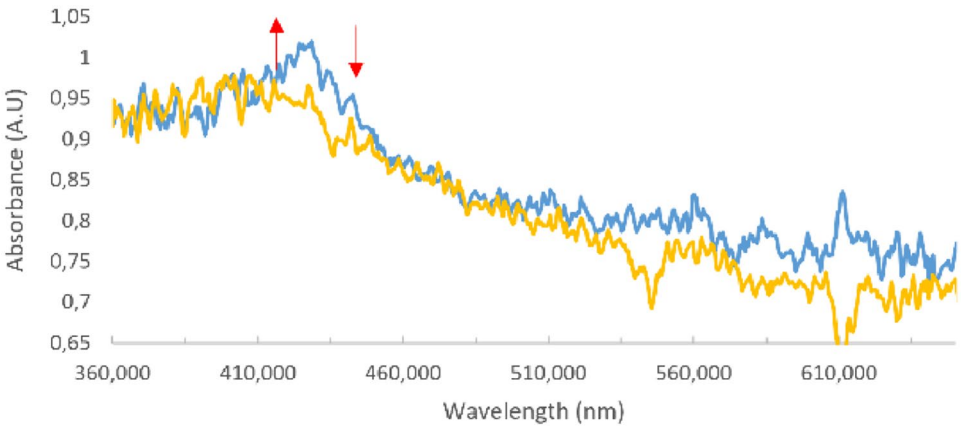

Fig. 6 Microcrystals of CcO (50–60 µM) in LCP mixed with caged oxygen compound **1** (2.5 mM) and DTT (15 mM) before (blue) and 1 ms after (yellow) a single laser pulse (5 ns, ~ 1 J/cm^2, 355 nm). Peak at 610 nm is not a spectral feature but a result from a noisy background and the spectral contribution from the caged oxygen compound **1** has been removed

carbon monoxide bound mixed-valence state of the enzyme [46] by incubating an aqueous solution of oxygen free of ba_3-type CcO with carbon monoxide gas over several hours. The addition of caged oxygen compound **1** lead to familiar issues with premature oxidation due to the thermal oxygen leakage, which in this case was not mitigated by the addition of the oxygen scrub system. Consequently, we shifted our attention to the more redox stable compound **3**. Despite its lower oxygen release potential, we rationalized that since the produced intermediate would be trapped due to a lack of further electrons to progress in the catalytic cycle, a lower concentration of O_2 would be tolerated during the experimental conditions. Also, by studying a slightly slower millisecond time point after the initial formation, sufficient oxygen should have had time to diffuse into the sample in the case that the initial oxygen burst is not enough to achieve a high population of reacted enzyme. Upon addition of compound **3** to a final concentration of 2 mM, no premature oxidation of CcO (120 µM) in the MVCO state was observed within 1 h. Upon exposure to a single 355 nm laser pulse, difference signals consistent with the formation of the $\mathbf{P_M}$ state were obtained. This is seen in Fig. 7 as a characteristic positive difference signal at 610 nm. Interestingly, this formed state was stable for about 30 s which was verified by exposing a stationary sample with a single laser pulse and recording spectrums over time. This demonstrates that a sufficiently high population of the $\mathbf{P_M}$ intermediate can be generated upon a single laser pulse at crystallographic relevant concentrations in an aqueous solution.

The work presented herein paves the way for the broader implementation of caged oxygen compounds in time-resolved studies, particularly applications towards serial crystallography. Our newly synthesized compounds **2** and **3** demonstrate a marked improvement in stability profiles, addressing the pervasive challenge of compound premature degradation under our desired experimental conditions. However, the fortification of stability is

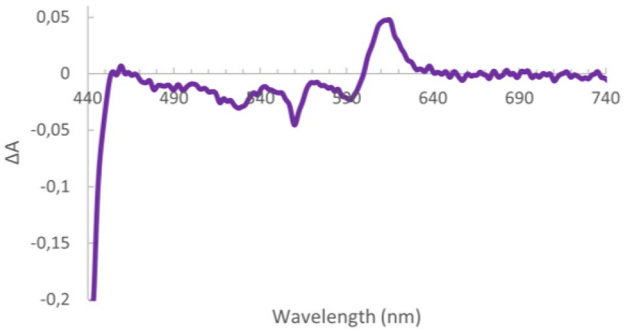

Fig. 7 Difference spectrum of carbon monoxide bound mixed valence Cytochrome *c* Oxidase (120 µM) and caged oxygen compound **3** (3 mM) as an aqueous solution, following a single laser pulse (5 ns, ~ 1 J/cm^2, 355 nm). The negative feature at 560 nm is a result of a slight over-reduction of the enzyme during preparation which is oxidized upon oxygen liberation. The spectral contribution of the caged oxygen compound has been removed and the spectrum was cut at 440 nm due to light saturation

accompanied by a compromise in the decreased efficiency of oxygen release. The ramifications of this are twofold. Enhanced stability extends the utility of these compounds, facilitating longer experimental durations with great improvements with regards to sample preparation, and minimizing the occurrence of premature degradation that could otherwise obscure accurate results. Conversely, the diminished efficiency requires an increased quantity of the compound, or the utilization of higher laser fluence, to accomplish the intended oxygen release levels. This interplay highlights the intricate equilibrium between stability and reactivity in the design of caged oxygen compounds. The protocol developed herein have been employed in a series of time-resolved X-ray investigations, the comprehensive findings of which will be delineated in subsequent publications.

3 Conclusion

In this study, we have successfully synthesized, characterized, and assessed several novel caged oxygen compounds, designed for advancing time-resolved studies of oxygen-depending systems. The presence of redox incompatibilities necessitated the development of an alternative reduction protocol, which has facilitated the general application of these compounds in experiments involving the reduced form of the CcO. Our experiments confirm that a single laser pulse is capable of liberating a significant amount of molecular oxygen from the caged compounds, sufficient to identify transient intermediates in the catalytic cycle of ba_3-type CcO at concentrations viable for further crystallographic analysis. Notably, compounds **2** and **3** exhibit enhanced redox stability, mitigating the limitations previously encountered with compound **1**, thus broadening the potential for application in systems that are necessitate reducing conditions. Furthermore, we present evidence for enzymatic turnover within microcrystals of reduced CcO, mediated by photoactive caged oxygen compounds.

Supplementary Information The online version contains supplementary material available at https://doi.org/10.1007/s43630-024-00558-x.

Acknowledgements This project received funding from the European Research Council (ERC) under the European Union's Horizon 2020 research and innovation programme (Grant agreement no 789030 to **RN**). This work was also supported by grants from the Swedish Research Council.

Funding Open access funding provided by University of Gothenburg.

Declarations

Conflict of interest On behalf of all authors, the corresponding author states that there is no conflict of interest.

References

1. Wallar, B. J., & Lipscomb, J. D. (1996). Dioxygen activation by enzymes containing binuclear non-heme iron clusters. *Chemical Reviews, 96*, 2625–2658. https://doi.org/10.1021/cr9500489
2. Gray, H. B., & Winkler, J. R. (2018). Living with oxygen. *Accounts of Chemical Research, 51*, 1850–1857. https://doi.org/10.1021/acs.accounts.8b00245
3. Lee, S. K., Froland, W. A., Lipscomb, J. D., et al. (1993). A transient intermediate of the methane monooxygenase catalytic cycle containing an FeIVFeIV cluster. *Journal of the American Chemical Society, 115*, 6450–6451. https://doi.org/10.1021/ja00067a086
4. Wikström, M., & Sharma, V. (2018). Proton pumping by cytochrome *c* oxidase—a 40 year anniversary. *Biochimica et Biophysica Acta Bioenergetics, 1859*, 692–698. https://doi.org/10.1016/j.bbabio.2018.03.009
5. Ferguson-Miller, S., & Babcock, G. T. (1996). Heme/copper terminal oxidases. *Chemical Reviews, 96*, 2889–2908. https://doi.org/10.1021/cr950051s
6. Van Eps, N., Szundi, I., & Einarsdottir, O. (2000). A new approach for studying fast biological reactions involving dioxygen: The reaction of fully reduced cytochrome *c* oxidase with O_2. *Biochemistry, 39*, 14576–14582. https://doi.org/10.1021/bi000955u
7. Szundi, I., Funatogawa, C., Fee, J. A., et al. (2010). CO impedes superfast O_2 binding in ba3 cytochrome oxidase from Thermus thermophilus. *Proceedings of National Academy of Sciences United States of America, 107*, 21010–21015. https://doi.org/10.1073/pnas.1008603107
8. Pearson, A. R., & Mehrabi, P. (2020). Serial synchrotron crystallography for time-resolved structural biology. *Current Opinion in Structural Biology, 65*, 1–7. https://doi.org/10.1016/j.sbi.2020.06.019
9. Siletsky, S. A., Belevich, I., Jasaitis, A., et al. (2007). Time-resolved single-turnover of ba3 oxidase from Thermus thermophilus. *Biochimica Biophysica Acta Bioenergetics, 1767*, 1383–1392. https://doi.org/10.1016/j.bbabio.2007.09.010
10. Mikšovská, J., & Larsen, R. W. (2003). Photothermal studies of the photodegradation of (μ-peroxo)(μ-hydroxo) bis[bis(bipyridyl) Co(III)] and (μ-peroxo)(μ-hydroxo) bis[bis(phenanthroline) Co(III)] complexes in water. *Inorganica Chimica Acta, 355*, 116–120. https://doi.org/10.1016/S0020-1693(03)00272-X
11. Kikkawa, M., Sasaki, Y., Kawata, S., et al. (1985). Photochemical and Thermal Decomposition of (ΔΔ, ΛΛ)-(μ-Hydroxo)(μ-peroxo) bis[bis(ethylenediamine)cobalt(III)] Ions in Basic Aqueous Solution. *Inorganic Chemistry, 24*, 4096–4100. https://doi.org/10.1021/ic00218a027
12. Ebihara, M., Sasaki, Y., & Saito, K. (1985). Mechanism of Acid-Catalyzed Decomposition of the (Δ & Delta, ΛΛ)-(μ-Hydroxo)(μ-peroxo)bis[bis(ethylenediamine)cobalt(III)] Ion. *Inorganic Chemistry, 24*, 3831–3835. https://doi.org/10.1021/ic00217a027
13. Kotani, H., Hong, D., Satonaka, K., et al. (2019). Mechanistic insight into dioxygen evolution from diastereomeric μ-peroxo dinuclear Co(III) complexes based on stoichiometric electron-transfer oxidation. *Inorganic Chemistry, 58*, 3676–3682. https://doi.org/10.1021/acs.inorgchem.8b03245
14. Ludovici, C., Fröhlich, R., Vogtt, K., et al. (2002). Caged O_2 reaction of cytochrome bo3 oxidase with photochemically released dioxygen from a cobalt peroxo complex. *European Journal of Biochemistry, 269*, 2630–2637. https://doi.org/10.1046/j.1432-1033.2002.02944.x
15. Einarsdóttir, Ó., Funatogawa, C., Soulimane, T., & Szundi, I. (2012). Kinetic studies of the reactions of O_2 and NO with reduced Thermus thermophilus ba3 and bovine aa3 using photolabile carriers. *Biochimica et Biophysica Acta, 1817*, 672–679.
16. Szundi, I., Funatogawa, C., Soulimane, T., & Einarsdóttir, Ó. (2020). The reactions of O_2 and NO with mixed-valence ba3 cytochrome *c* OXIDASE from Thermus thermophilus. *Biophysical Journal, 118*, 386–439. https://doi.org/10.1016/j.bpj.2019.11.3390
17. Macarthur, R., Sucheta, A., Chongt, F. F. S., & Einarsdottir, O. (1995). Photodissaciation of a (μ-peroxo)(μ-hydroxo)

bis[bis(bipyridyl)-cobalt(III) J complex: A tool to study fast biological reactions involving 02. *PNAS, 92*, 8105–8109.
18. Olmos, J. L., Pandey, S., Martin-Garcia, J. M., et al. (2018). Enzyme intermediates captured 'on the fly' by mix-and-inject serial crystallography. *BMC Biology, 16*, 1–15.
19. Ishigami, I., Lewis-Ballester, A., Echelmeier, A., et al. (2019). Snapshot of an oxygen intermediate in the catalytic reaction of cytochrome *c* oxidase. *Proceedings of National Academy of Sciences United States of America, 116*, 3572–3577. https://doi.org/10.1073/pnas.1814526116
20. Brändén, G., & Neutze, R. (2021). Advances and challenges in time-resolved macromolecular crystallography. *Science, 373*, 1–13.
21. Orville, A. M. (2020). Recent results in time resolved serial femtosecond crystallography at XFELs. *Current Opinion in Structural Biology, 65*, 193–208. https://doi.org/10.1016/j.sbi.2020.08.011
22. Brändén, G., & Neutze, R. (2021). Advances and challenges in time-resolved macromolecular crystallography. *Science, 373*, 1–13. https://doi.org/10.1126/SCIENCE.ABA0954/ASSET/4C9C3E09-F268-4D7B-9E4E-F70396F031FD/ASSETS/IMAGES/LARGE/SCIENCE.ABA0954-F6.JPG
23. Monteiro, D. C. F., Amoah, E., Rogers, C., & Pearson, A. R. (2021). Using photocaging for fast time-resolved structural biology studies. *Acta Crystallographica Section D Structural Biology, D77*, 1218–1232. https://doi.org/10.1107/S2059798321008809
24. Josts, I., Niebling, S., Gao, Y., et al. (2018). Photocage-initiated time-resolved solution X-ray scattering investigation of protein dimerization. *IUCrJ, 5*, 667–672. https://doi.org/10.1107/S2052252518012149
25. Nomura, T., Kimura, T., Kanematsu, Y., et al. (2021). Short-lived intermediate in N_2O generation by P450 NO reductase captured by time-resolved IR spectroscopy and XFEL crystallography. *Proceedings of National Academy Sciences United States of America, 118*, 1–5. https://doi.org/10.1073/pnas.2101481118
26. Mehrabi, P., Schulz, E. C., Dsouza, R., et al. (2019). Time-resolved crystallography reveals allosteric communication aligned with molecular breathing. *Science, 365*, 1167–1170. https://doi.org/10.1126/science.aaw9904
27. Andersson, R., Safari, C., Dods, R., et al. (2017). Serial femtosecond crystallography structure of cytochrome *c* oxidase at room temperature. *Science and Reports, 7*, 4518. https://doi.org/10.1038/s41598-017-04817-z
28. Ghosh, S., Zoric, D., Dahl, P., et al. (2023). A simple goniometer-compatible flow cell for serial synchrotron X-ray crystallography. *Journal of Applied Crystallography, 56*, 56. https://doi.org/10.1107/S1600576723001036
29. Safari, C., Ghosh, S., Andersson, R., et al. (2023). Time-resolved serial crystallography to track the dynamics of carbon monoxide in the active site of cytochrome *c* oxidase. *Science Advances, 9*, 1–12. https://doi.org/10.1126/sciadv.adh4179
30. Smirnova, I., Chang, H. Y., Von Ballmoos, C., et al. (2013). Single mutations that redirect internal proton transfer in the ba 3 oxidase from thermus thermophilus. *Biochemistry, 52*, 7022–7030. https://doi.org/10.1021/bi4008726
31. Bogucki, R. F., McLendon, G., & Martell, A. E. (1976). Oxygen complexation by cobaltous chelates of multidentate pyridyl-type ligands. Equilibria, reactions, and electron structure of the complexes. *Journal of the American Chemical Society, 98*, 3202–3205. https://doi.org/10.1021/ja00427a024
32. Harris, W. R., Timmons, J. H., & Martellt, A. E. (1979). Stabilities of monobridged binuclear cobalt dioxygen complexes: A linear free energy relationship. *Journal of Coordination Chemistry, 8*, 251–253. https://doi.org/10.1080/00958977908076506
33. Vaska, L. (1976). Dioxygen-metal complexes: Toward a unified view. *Accounts of Chemical Research, 9*, 175–183. https://doi.org/10.1021/ar50101a002
34. Shankar, K., & Baruah, J. B. (2017). A stable peroxo- and hydroxido-bridged dinuclear cobalt(III) ethylenediammine 2,4-dinitrophenolate complex. *Inorganic Chemistry Communications, 84*, 45–48. https://doi.org/10.1016/j.inoche.2017.07.006
35. Miskowski, V. M. (1987). The electronic spectra of μ-Peroxodicobalt(lll) complexes. *Comments on Inorganic Chemistry, 6*, 193–207. https://doi.org/10.1080/02603598708072290
36. Lever, A. B. P., Ozin, G. A., & Gray, H. B. (1980). Electron transfer in metal-dioxygen adducts. *Inorganic Chemistry, 19*, 1823–1824. https://doi.org/10.1021/ic50208a085
37. Teng, Q., & Huynh, H. V. (2017). A unified ligand electronic parameter based on 13C NMR spectroscopy of N-heterocyclic carbene complexes. *Dalton Transactions, 46*, 614–627. https://doi.org/10.1039/c6dt04222h
38. Montalti, M., Credi, A., Prodi, L., & Teresa Gandolfi, M. (2006). Chemical actinometry. In B. Raton (Ed.), *Handbook of photochemistry* (3rd ed., pp. 601–616). Taylor & Francis Group, LLC.
39. Levantino, M., Yorke, B. A., Monteiro, D. C. F., et al. (2015). Using synchrotrons and XFELs for time-resolved X-ray crystallography and solution scattering experiments on biomolecules. *Current Opinion in Structural Biology, 35*, 41–48. https://doi.org/10.1016/j.sbi.2015.07.017
40. Pegis, M. L., Wise, C. F., Martin, D. J., & Mayer, J. M. (2018). Oxygen reduction by homogeneous molecular catalysts and electrocatalysts. *Chemical Reviews, 118*, 2340–2391. https://doi.org/10.1021/acs.chemrev.7b00542
41. Bowers, P. G., Hofstetter, C., Letter, C. R., & Toomey, R. T. (1995). Supersaturation limit for homogeneous nucleation of oxygen bubbles in water at elevated pressure: 'Superhenry's law.' *Journal of Physical Chemistry, 99*, 9632–9637. https://doi.org/10.1021/j100023a048
42. Swoboda, M., Henig, J., Cheng, H. M., et al. (2012). Enzymatic oxygen scavenging for photostability without ph drop in single-molecule experiments. *ACS Nano, 6*, 6364–6369. https://doi.org/10.1021/nn301895c
43. Andersson, R., Safari, C., Bath, P., et al. (2019). Well-based crystallization of lipidic cubic phase microcrystals for serial X-ray crystallography experiments. *Acta Crystallographica Section D Structural Biology, 75*, 937–946. https://doi.org/10.1107/S2059798319012695
44. Shimazu, Y., Tono, K., Tanaka, T., et al. (2019). High-viscosity sample-injection device for serial femtosecond crystallography at atmospheric pressure. *Journal of Applied Crystallography, 52*, 1280–1288. https://doi.org/10.1107/S1600576719012846/TE5044SUP2.PDF
45. Von Der Hocht, I., Van Wonderen, J. H., Hilbers, F., et al. (2011). Interconversions of P and F intermediates of cytochrome *c* oxidase from Paracoccus denitrificans. *Proceedings of National Academy Science United States of America, 108*, 3964–3969. https://doi.org/10.1073/PNAS.1100950108/SUPPL_FILE/PNAS.1100950108_SI.PDF
46. Wikström, M., Gennis, R. B., & Rich, P. R. (2023). Structures of the intermediates in the catalytic cycle of mitochondrial cytochrome *c* oxidase. *Biochimica et Biophysica Acta Bioenergetics, 1864*, 148933. https://doi.org/10.1016/j.bbabio.2022.148933